Chapter 3

CFD Modelling of Oxy-Coal Combustion in a Tubular Combustor

3.1 Overview

This chapter presents a detailed computational modelling methodology of oxy-coal combustion. The models/submodels employed for CFD investigation of oxy-coal combustion has been thoroughly discussed. In the second part of the chapter, the grid independence study and validation of developed numerical models with the experimental results of Toporov et al. (2008) and numerical Large Eddy Simulation (LES) results of Warzecha and Boguslawski (2014a) have been presented.

3.2 Theoretical Formulation and Operating Condition

Physical model of the research problem refers to oxy-fuel combustion of lignite coal in the vertical cylindrical combustor of Heat and Mass transfer at RWTH Aachen University. The diameter and length of the cylindrical combustion chamber are 0.4 m and 2.1 m, as displayed in Fig. 3.1(a). Swirl oxy-coal burner dimensions can be seen in Fig. 3.1 (b). There are four inlets in the oxy-coal furnace. From the first inlet, the primary stream transports the pulverized coal into the combustor. Injection co-ordinate for coal particles are selected in the opening range of inlet 1, and the injection velocity is specified (in

discrete phase modelling) identical to the primary stream velocity. The second inlet is used to inject the swirling secondary stream into the combustor with the swirl number $S = (v_{tan}/v_{ax})$ equal to 1 (Heil et al., 2009). Third and fourth inlets are used for injecting tertiary and staging stream into the combustor through the top wall of the furnace. The tertiary stream is injected for scavenging purpose whereas, the staging stream is used to maintain the stoichiometry of the burner by decreasing the gas injected as primary and secondary streams.
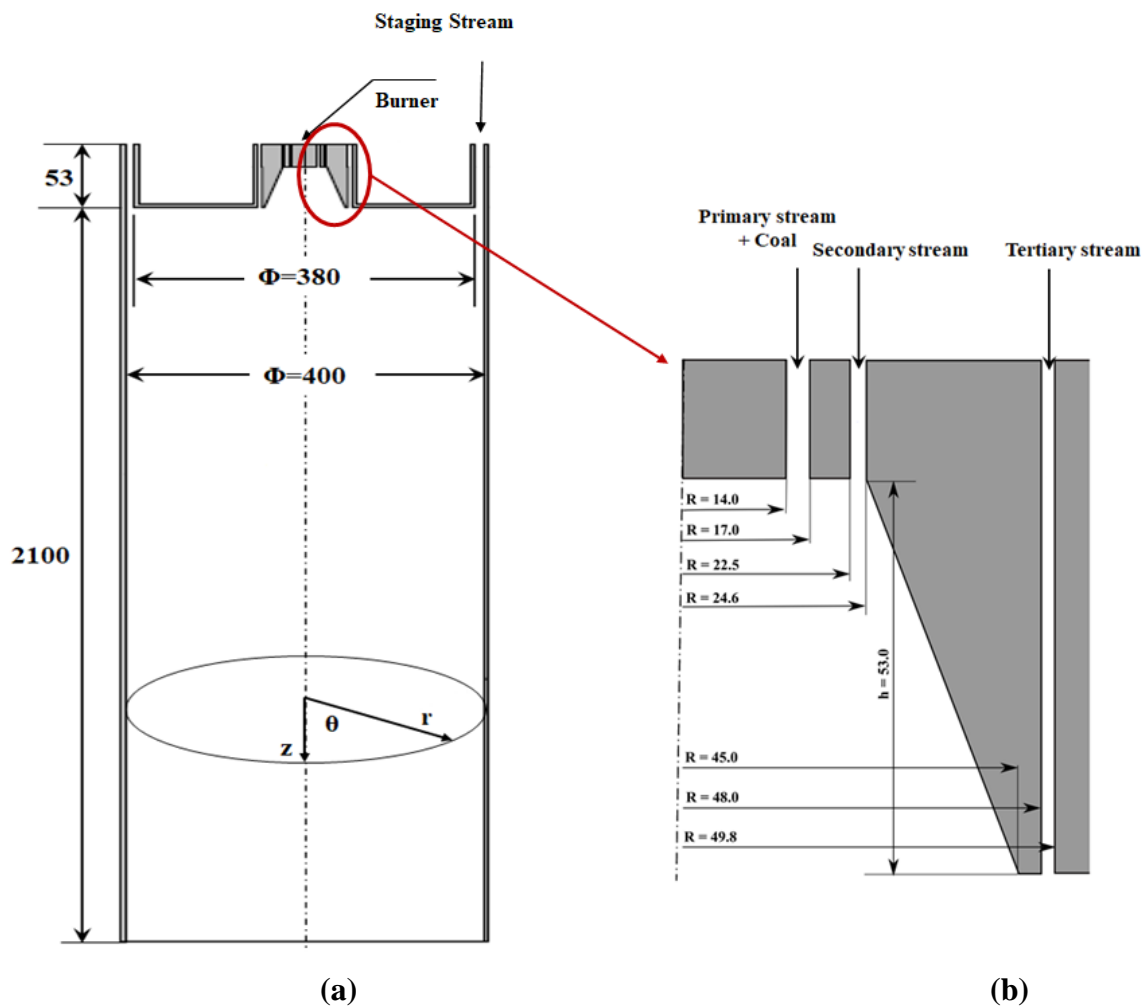
Fig. 3.1. The geometry of **(a)** oxy-fuel furnace and **(b)** swirl burner (all dimensions are in mm)

Table 3.1 Operating condition of oxy-coal test facility

	Flow rate (kg/h)	O_2 (% vol.)	CO_2 (% vol.)	Temperature (K)
Coal	6.5	-	-	313
Primary stream (inlet 1)	17.6	19	81	313
Secondary stream (inlet 2)	26.6	21	79	333
Tertiary stream (inlet 3)	1.5	21	79	333
Staging stream (inlet 4)	54.9	21	79	1173
Burner temperature	_	_	_	573
Wall temperature	_	_	_	1273

Table 3.2 Lignite coal composition used in numerical study

Proximate analysis (%)		Ultimate analysis (%) DAF	
Moisture	8.4	Carbon	77.03
Ash	4.1	Hydrogen	4.85
Volatiles	46.6	Nitrogen	0.98
Char	40.9	Sulfur	0.34
		Oxygen	16.80

The experimental investigation of oxy-coal combustion test facility has been conducted by the Toporov et al. (2008)**.** We have adopted the oxy-coal combustion test facility along with its boundary and operating conditions for the current numerical investigation. The operating conditions and coal proximate and ultimate analysis data employed by Toporov et al. (2008) in the experimental investigation are provided in Table 3.1 and Table 3.2, respectively.

3.3 Computational Modelling

Computational fluid dynamics (CFD) simulations have been performed to describe the reactive flow field, temperature distribution and species concentration profile in the combustor. The Eulerian-Lagrangian method has been employed for continuous and particulate phase modelling. Coupling between continuous and particulate phases has been performed by interactive source terms. Owing to the smaller size (diameter) of pulverized coal particles, the buoyancy and body forces on the particle are not considered. The virtual mass force and Basset force are also not considered due to the higher density ratio of gaseous and particle phases. Ansys Fluent 19.0 has been used to model oxy-coal combustion. The steady-state governing equations are solved by employing pressure based 2 D axisymmetric solver. It has been found from the computation studies available in the literature that the axisymmetric solver is able to model pulverized coal swirl flame with lower computational cost without losing accuracy. That's why the axisymmetric solver has been used in numerous numerical modelling studies of swirling oxy-coal flame (Gaikwad et al., 2017; Hu and Yan, 2013; Jovanović et al., 2019, 2014, 2017; Yin, 2017). Hence, the use of 2D axisymmetric solver is completely justified for the symmetrical geometry and expected flow field symmetry (Jovanovic et al., 2012).

The SIMPLE scheme has been used for Pressure-velocity coupling. The governing equations are solved by the second-order upwind scheme. For the modelling of turbulence, RANS based standard k-ε, RNG k-ε, realizable k-ε and SST k-ω turbulence models have been selected. For inlet and outlet boundary conditions, mass flow inlet and pressure outlet conditions have been selected. Radiation heat transfer in oxy-coal combustion atmosphere

is modelled by using discrete ordinate (DO) model. The weighted sum gray gas model (WSGGM) is coupled with the discrete ordinate (DO) model for the computation of the absorption coefficient of gray gases. The model coefficients of WSGGM are developed for air-fired combustion by Smith et al. (1982). These model coefficients are modified by Johansson et al. (2010) for oxy-coal combustion. We have implemented the modified model coefficients of Johansson et al. (2010) in the solver through user-defined function (UDF). The turbulence-chemistry interactions have been considered by the finite rate/eddy dissipation model (FR/EDM). In FR/EDM, Arrhenius rate and eddy dissipation reaction rates are limited by the chemical kinetics and turbulent mixing, respectively. The net reaction rate is the lower value of these two rates.

Rosin-Rammler distribution is used to group PC particles (0.9-123 µm) into the adequate number of sizes. Discrete random walk model (DRW) has been employed for the modelling of particles turbulent dispersion. Particle force balance equation is solved to obtain the trajectories of pulverized coal particles. The particle energy equation is solved for the estimation of particle temperature. The single kinetic rate model (Badzioch and Hawksley, 1970) is employed for the modelling of devolatilization behaviour of coal particles. The model coefficients of devolatilization model are taken from the literature (Gaikwad et al., 2017; Warzecha and Boguslawski, 2014a). The kinetic/diffusion-limited rate model is employed for the modelling of heterogeneous reactions at the char surface. The swirl intensity of the secondary stream is characterized by swirl number (S). The swirl number (S) is defined as the axial flux of tangential momentum to the axial flux of axial momentum.

$$G_\phi = \rho Q \overline{U}_\theta r \qquad\qquad\qquad (3.1)$$

$$G_x = \rho Q \overline{U}_z \qquad\qquad\qquad (3.2)$$

$$S = \frac{G_\phi}{G_x r_0} \qquad\qquad\qquad (3.3)$$

where ρ, Q, $\overline{U}_z$ and $\overline{U}_\theta$ represent density (kg/m^3), volume flow rate (m^3/s), axial velocity (m/s) and tangential velocity (m/s) respectively. r and r_0 represent gas rotation radius (m) and characteristic scale (m).

The tangential and axial velocity ratios are derived from the swirl number definition. The value of ($\overline{U}_\theta / \overline{U}_z$) is used as inlet boundary conditions for each swirl number S. Section 4.2 of Chapter 4 summarizes the influence of swirl strength on the flow and combustion properties. For other sections except section 4.2, swirl number S=1 has been considered.

3.3.1 Continuous Phase Modelling

The Eulerian approach has been used to model the continuous phase. The mass, momentum, species and energy conservation equations have been solved to describe reactive flow field. The concentrations of volatiles, hydrogen, nitrogen, carbon monoxide, sulfur dioxide, water vapor and oxygen have been calculated by solving their species conservation equation. The concentration of carbon dioxide has been estimated by employing mass balance.

The Conservation of Mass (Continuity Equation)

$$\frac{\partial \rho}{\partial t} + \frac{\partial}{\partial x_i}\left(\rho \overline{U}_i\right) = \dot{S} \qquad\qquad\qquad (3.4)$$

The Momentum Conservation Equation

$$\frac{\partial(\rho\overline{U}_i)}{\partial t} + \frac{\partial}{\partial x_j}\left(\rho\overline{U}_i\overline{U}_j\right) = -\frac{\partial p'}{\partial x_i} + \frac{\partial}{\partial x_j}\left\{\mu_{eff}\left(\frac{\partial\overline{U}_i}{\partial x_j} + \frac{\partial\overline{U}_j}{\partial x_i}\right)\right\} + \dot{S}_{M_i} + \dot{S}\,\overline{U}_i \qquad (3.5)$$

where $\quad \mu_{eff} = \mu + \rho c_\mu \dfrac{k^2}{\varepsilon}$ $\qquad\qquad\qquad\qquad\qquad\qquad\qquad\qquad$ (3.6)

$$p' = p + \frac{2}{3}\rho k + \frac{2}{3}\mu_{eff}\frac{\partial\overline{U}_j}{\partial x_j} \qquad\qquad\qquad\qquad\qquad (3.7)$$

Turbulence model

Reynolds Average Navier Stokes (RANS) based turbulence models have been used to compute the convection and diffusion of turbulent energy. The k-ε model has been most frequently employed to model the turbulent flow of a wide variety of computational problems. The transport equations for turbulence kinetic energy k and turbulent dissipation rate ε are solved in the k-ε model. The standard k-ε (Launder and Spalding, 1972), Realizable k-ε (Shih et al., 1995) and RNG k-ε (Orszag et al., 1993) model solve the similar type of transport equations. The difference in these models is found mainly in the calculation method of turbulent viscosity μ_t. The transport equation for 'ε' is based on the dynamic equation of mean square vorticity fluctuations in Realizable k-ε model. The Realizable k-ε model also makes use of the variable value of constant C_μ in the computation of turbulent viscosity μ_t. Hence, the Realizable k-ε can be used for accurate prediction of flows with recirculation and separation. The RNG k-ε model has an additional term of 'ε' transport equation. The RNG k-ε model considers the influence of swirl on turbulence and can be used for accurate prediction of rapidly strained flows.

Transport equation of turbulent kinetic energy (K)

$$\frac{\partial(\rho k)}{\partial t} + \frac{\partial}{\partial x_i}\left(\rho \overline{U}_i k\right) = \frac{\partial}{\partial x_i}\left[\left(\mu + \frac{\mu_t}{\sigma_k}\right)\frac{\partial k}{\partial x_i}\right] + G_k + G_b - \rho\varepsilon - Y_M + \dot{S}k \tag{3.8}$$

Transport equation of turbulent dissipation rate (ε)

$$\frac{\partial(\rho\varepsilon)}{\partial t} + \frac{\partial}{\partial x_i}\left(\rho \overline{U}_i \varepsilon\right) = \frac{\partial}{\partial x_i}\left[\left(\mu + \frac{\mu_t}{\sigma_\varepsilon}\right)\frac{\partial \varepsilon}{\partial x_i}\right] + c_{1\varepsilon}\frac{\varepsilon}{k}\left(G_k + C_{3\varepsilon}G_b\right) - \rho c_{2\varepsilon}\frac{\varepsilon^2}{k} + \dot{S}\varepsilon \tag{3.9}$$

$$\mu_t = \rho C_\mu \frac{k^2}{\varepsilon} \tag{3.10}$$

The transport equations for turbulent kinetic energy 'k' and specific dissipation rate 'ω' are solved in the k-ω model to compute the turbulent viscosity μ_t. The transport equations for k and ω are:

$$\frac{\partial(\rho k)}{\partial t} + \frac{\partial}{\partial x_i}\left(\rho \overline{U}_i k\right) = \frac{\partial}{\partial x_i}\left[\left(\mu + \frac{\mu_t}{\sigma_k}\right)\frac{\partial k}{\partial x_i}\right] + G_k - Y_k + Sk \tag{3.11}$$

$$\frac{\partial(\rho\omega)}{\partial t} + \frac{\partial}{\partial x_i}\left(\rho \overline{U}_i \omega\right) = \frac{\partial}{\partial x_i}\left[\left(\mu + \frac{\mu_t}{\sigma_\omega}\right)\frac{\partial \omega}{\partial x_i}\right] + G_\omega - Y_\omega + \dot{S}\varepsilon \tag{3.12}$$

$$\mu_t = a * \frac{\rho k}{\omega} \tag{3.13}$$

The SST k-ω model (Menter, 1994) is able to predict swirl flow and adverse pressure gradient flow due to its inherent advantage. This model works as standard k-ε in the far-field region and standard k-ω model in the near-wall region by employing a cross diffusive term and appropriate blending function.

Energy Conservation Equation

The equation for energy conservation in the form of enthalpy is written as

$$\frac{\partial(\rho h)}{\partial t} + \frac{\partial}{\partial x_i}(\rho \overline{U}_i h) = \frac{\partial}{\partial x_i}\left(\rho \alpha_t \frac{\partial h}{\partial x_i}\right) - \dot{S}_E - \frac{\partial q_{ri}}{\partial x_i} + \dot{S}h \qquad (3.14)$$

$\dot{S}_E$ is the absorbed energy from the gaseous phase by the pulverized coal particles and q_{ri} is radiative heat flux contributed due to heat transfer between particle and gas phase.

Radiation model

Radiative transfer equation (RTE) has been solved and coupled with the model of radiation properties for the computation of the radiation heat transfer inside the combustion chamber. The Radiative transfer equation at position $\vec{r}$ in direction $\vec{s}$ is given as:

$$\frac{dI_\lambda(\vec{r},\vec{s})}{ds} = k_\lambda n^2 I_{b\lambda} - (k_\lambda + \sigma_{s,\lambda})I_\lambda(\vec{r},\vec{s}) + \frac{\sigma_{s,\lambda}}{4\pi}\int_{\Omega=0}^{4\pi} I_\lambda(\vec{r},\vec{s'})\Phi(\vec{s}.\vec{s'})d\Omega' \qquad (3.15)$$

In the current work, the radiative transfer equation (RTE) has been solved by the discrete ordinate (DO) model (Chui and Raithby, 1993).

The radiative transfer equation (RTE) can be simplified by

$$\frac{dI_\lambda(\vec{r},\vec{s})}{ds} = k_\lambda n^2 I_{b\lambda} - k_\lambda I_\lambda(\vec{r},\vec{s}) \qquad (3.16)$$

By integrating radiation intensity over full radiation spectrum

$$\frac{dI(\vec{r},\vec{s})}{ds} = \overline{a}n^2 \frac{\sigma T^4}{\pi} - \overline{a}_{incident}I(\vec{r},\vec{s}) \qquad (3.17)$$

Where $\overline{a}$ and $\overline{a}_{incident}$ represent Planck's mean absorption coefficient, and incident mean absorption coefficient, respectively. The absorption coefficients are averaged over full spectrum weighted by radiation intensity. The absorption coefficients are function of

temperature, pressure and gas composition. The absorption coefficient prediction is computationally complex. Hence, the absorption property-based band or gray gas models are most commonly utilized for the modelling of radiative heat transfer. The weighted sum of gray gases model (WSGGM) proposed by Smith et al. (1982) is the most frequently utilized gray gas model. WSGGM Model Parameters are based on flue gas radiative properties under conventional air combustion. The WSGGM assumes that the gas consists of a transparent gas and several gray gases without any wavelength dependence.

WSGGM determines the Planck's mean absorption coefficient of the gas mixture over a path length $\vec{s}$ by

$$\bar{a} = -\ln(1-\varepsilon)/s \tag{3.18}$$

Where s is beam length of radiation and ε is emissivity of gas. The value of radiation beam length is estimated to be 0.6 based on computational domain dimensions whereas gas emissivity is calculated as

$$\varepsilon = \sum_i a_{\varepsilon,i}(T)(1 - \exp(-k_i p_i s)) \tag{3.19}$$

Where $a_{\varepsilon,i}$ represents the weighting factor of emissivity for gray gas i. p_i and k_i represents the partial pressure and pressure absorption coefficient of absorbing gas i. The emissivity weight factor $a_{\varepsilon,i}$ is function of temperature and given by polynomial correlations. The sets of coefficients are computed by proposed model of Johansson et al. (2010) for WSGGM under oxy-fuel combustion for different CO_2/H_2O ratio.

$$a_{\varepsilon,i} = \sum_j b_{\varepsilon,i,j} \left(\frac{T}{T_{ref}} \right)^{j-1} \tag{3.20}$$

Where $b_{\varepsilon,i,j}$ and T_{ref} represent the emissivity gas temperature polynomial coefficients and reference temperature, respectively. The coal particles also contribute to the radiation heat transfer and its contribution is included in RTE by absorption and scattering coefficient of coal particle. The absorption coefficient k_i and emissivity gas temperature polynomial coefficients $b_{\varepsilon,i,j}$ are computed as

$$k_i = K_{1,i} + K_{2,i} \frac{Y_{H_2O}}{Y_{CO_2}} \tag{3.21}$$

$$b_{\varepsilon,i,j} = C1_{i,j} + C2_{i,j} \frac{Y_{H_2O}}{Y_{CO_2}} + C3_{i,j} \left(\frac{Y_{H_2O}}{Y_{CO_2}} \right)^2 \tag{3.22}$$

The coefficient for $K_{1,i}$, $K_{2,i}$, $C1_{i,j}$, $C2_{i,j}$ and $C3_{i,j}$ are provided by Johansson et al. (2010) for Y_{H_2O}/Y_{CO_2} ranges from 0.125 to 2. The value of absorption coefficient k_i and polynomial coefficients $b_{\varepsilon,i,j}$ are implemented in Fluent solver through the user defined function (UDF).

Conservation equation of species

$$\frac{\partial}{\partial t}(\rho Y_i) + \frac{\partial}{\partial x_i}\left(\rho \overline{U}_i Y_i\right) = \frac{\partial}{\partial x_i}\left(\rho D \frac{\partial Y_i}{\partial x_i}\right) + R_i + \dot{S}_i \tag{3.23}$$

Where R_i and S_i represent net rate of production of species i by chemical reaction and rate of creation by addition from dispersed phase, respectively.

Gas phase reaction modelling

The finite rate/eddy dissipation model (ER/EDM) is used to model the turbulent chemistry interactions. The smaller of kinetic rate and species turbulent mixing rate is considered as controlling reaction rate. The smaller of the reactant mixing rate and product mixing rate

utilized for the calculation of net rate of production of species i due to reaction r, $R_{i,r}$ in EDM (Magnussen and Hjertager, 1977).

Finite kinetic Arrhenius rate expression

$$R_{i,r} = \Gamma\left(v_{i,r}^{''} - v_{i,r}^{'}\right)\left[k_{f,r}\prod_{j=1}^{N} C_{j,r}^{\left(\eta_{j,r}^{'} + \eta_{j,r}^{''}\right)}\right] \tag{3.24}$$

$$k_{f,r} = A_r T^{\beta} e^{-(E/RT))} \tag{3.25}$$

Where $v_{i,r}^{'}$ and $v_{i,r}^{''}$ represent stoichiometric coefficient for reactant and product i in reaction r. $\eta_{j,r}^{'}$ and $\eta_{j,r}^{''}$ represent rate exponent for reactant and product species j in reaction r. $C_{j,r}$ is the molar concentration of species j in reaction r. A_r, E, β and R represent pre-exponential factor, activation energy, temperature exponent and universal gas constant, respectively.

Eddy dissipation model (EDM) expression

$$R_{i,r} = v_{i,r}^{'} M_{w,i} A\rho \frac{\varepsilon}{k} \min R\left(\frac{Y_R}{v_{R,r}^{'} M_{w,R}}\right) \tag{3.26}$$

$$R_{i,r} = v_{i,r}^{'} M_{w,i} AB\rho \frac{\varepsilon}{k} R\frac{\sum_P Y_P}{\sum_j^N v_{j,r}^{''} M_{w,j}} \tag{3.27}$$

When coal particles are heated, the volatile matter is released from coal in the gas phase. Eq[n] (3.28-3.30) represent the homogeneous combustion reactions of volatiles in the gas phase. These gas phase reactions along with their kinetic parameters are implemented in the solver.

$$C_x H_y O_z N_m S_n + \left(\frac{x}{2} + n - \frac{z}{2}\right)O_2 \rightarrow xCO + \frac{y}{2}H_2 + nSO_2 + \frac{m}{2}N_2 \tag{3.28}$$

$$2CO + O_2 \rightarrow 2CO_2 \tag{3.29}$$

$$2H_2 + O_2 \rightarrow 2H_2O \tag{3.30}$$
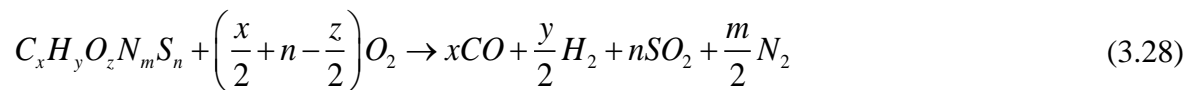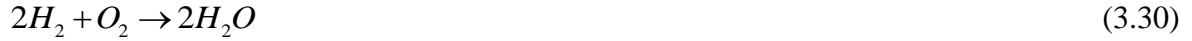
The proximate and ultimate analysis data of coal have the values of x, y, z, m and n used in eq^n (3.28). The kinetic data these gas phase combustion reactions are summarized in Table 3.3.

3.3.2 Modelling of Particle Phase

Distribution of particles

Rosin Rammler distribution (Rosin and Rammler, 1933) is used to group pulverized coal particles into the adequate number of sizes.

$$G'(d_i) = \frac{\exp\left(-bd_i^n\right) - \exp\left(-bd_{\max,i}^n\right)}{\exp\left(-bd_{\min,i}^n\right) - \exp\left(-bd_{\max,i}^n\right)} \tag{3.31}$$

Table 3.4 provides the size distribution of pulverized coal particles having a minimum diameter, maximum diameter, mean diameter and spread parameter 0.9 µm, 123 µm, 60 µm and 3.5, respectively.

Particle velocity

$$m_p \frac{dV_i}{dt} = \frac{\pi}{8} \rho d_p^2 C_D |U_i - V_i|(U_i - V_i) \tag{3.32}$$

Where C_D is drag coefficient computed by using standard drag law from literature (Clift et al., 1978).

Stochastic approach is used for the investigation of effect of gas phase turbulence on particle motion. The instantaneous gas phase velocity (U_i) is computed by the fluctuating

component of velocity from the turbulent kinetic energy in consideration of isotropic turbulence and using a normally distributed random number ζ as

$$U_i = \overline{U}_i + \zeta \frac{2k}{3} \tag{3.33}$$

Movement of particle in gas phase is traced by updating their position from the equation

$$\frac{dx_i}{dt} = V_i \tag{3.34}$$

Particle temperature

$$m_p c_p \frac{dT_p}{dt} = hA_p \left(T_g - T_p\right) + \varepsilon_p A_p \sigma \left(\theta_R^4 - T_p^4\right) - \frac{dm_{vol}}{dt} \Delta H_{devo} + \frac{dm_{char}}{dt} \Delta H_{char} \tag{3.35}$$

The convective heat transfer coefficient is computed from the literature (Ranz and Marshall, 1952) as

$$Nu = \frac{hd_p}{k} = 2.0 + 0.6 \, \text{Re}_p^{0.5} \, \text{Pr}^{0.33} \tag{3.36}$$

Modelling of coal devolatilization

During the devolatilization process, the release of volatile matter into the gaseous phase takes place. Devolatilization is an endothermic process which takes place during the preliminary stage of coal combustion and affects flame stability, temperature profile and emission. Devolatilization models are used for the prediction of the rate at which volatile matter evolves and releases from the coal.

The thermal decomposition of pulverized coal particle has been dealt with the single kinetic rate model (Badzioch and Hawksley, 1970). The single kinetic rate model recommends that

the devolatilization rate is the first order dependent on the amount of volatile remained in the particle. The rate of devolatilization is computed by Arrhenius expression.

$$-\frac{dm_p}{dt} = k\left[m_p - \left(1 - f_{v,0}\right)(1 - f_{w,0})m_{p,0}\right]$$

(3.37)

Where $m_{p,0}$, $f_{v,0}$ and $f_{w,0}$ represent initial particle mass, initial volatile mass fraction and initial moisture mass fraction, respectively present in coal. The devolatilization rate constant 'k' is given by

$$k = Ae^{-(E/R_u T_p)}$$

(3.38)

The pre-exponential coefficient, A=2.0e+05 and activation energy E=4.9e+07 J/kmol are taken from the literature (Gaikwad et al., 2017; Warzecha and Boguslawski, 2014a).

Oxy-char combustion modelling

The volatile matter and light gases are released from coal particle during the devolatilization process; hence, the residual mass obtained which is enriched in carbon and have some traces of sulphur, nitrogen and mineral matter termed as char. The consumption of coal char takes place by heterogeneous oxidation and gasification reactions at the char particle surface. These heterogeneous reactions are given below. These heterogeneous reactions, along with their kinetic parameters, are implemented in the solver.

$$C_{(s)} + \frac{1}{2}O_2 \rightarrow CO$$

(3.39)

$$C_{(s)} + CO_2 \rightarrow 2CO$$

(3.40)

$$C_{(s)} + H_2O \rightarrow CO + H_2$$

(3.41)

The char reaction rate of oxy-char combustion reactions is given as

$$\dot{m}_p = -A_p P_i \frac{D_i R_i}{D_i + R_i} \tag{3.42}$$

Where A_p and P_i are the external surface area of char particle and partial pressure of species i in the bulk gas. The surface reaction kinetic rate, R_i, in the Arrhenius form is represented as

$$R_i = A_i T_p^{\beta} \exp\left(-\frac{E}{R_u T_p}\right) \tag{3.43}$$

The diffusion limited reaction rate, D_i, is given as

$$D_i = C_i \frac{\left[(T_p + T_\infty)/2\right]^{0.75}}{d_p} \tag{3.44}$$

Where d_p and C_i are particle diameter and mass diffusion limited constant, respectively. T_p and T_∞ represent temperature of particle and gas phase, respectively. The kinetic data of both homogeneous and heterogeneous reactions summarized in Table 3.3.

Table 3.3 Kinetic parameters for homogeneous and heterogeneous reactions (Toporov et al., 2008; Warzecha and Boguslawski, 2014a)

Equation number	Pre-exp. factor	Activation energy (J/kmol)	Temperature exp.
Homogenous reactions			
(3.28)	1.6e+06	5.065e+07	0
(3.29)	5.42e+09	1.26e+08	0
(3.30)	1e+15	1e+08	0
Heterogeneous reactions			
(3.39)	0.005	7.4e+07	0
(3.40)	0.006351	1.62e+08	0
(3.41)	0.00192	1.47e+08	0

Table 3.4 Particle size distribution of Rhenish lignite coal

Diameter (d) [μm]	Mass fraction > d [%]
123	0.05139
109	0.05539
95.9	0.19439
82.3	1.9054
68.7	10.714
55.2	32.70
41.6	62.44
28	86.145
14.5	97.388
0.9	99.92

3.3.3 Interphase Source Interaction Terms

The source interaction terms appearing in the gas phase conservation equations are determined as follows

$$\dot{S} = \sum_{k=1}^{r} \frac{1}{\forall} \frac{d}{dt} \left(m_p(k) \right) \dot{N}(k) \Delta t \tag{3.45}$$

$$\dot{S}_{M_i} = \sum_{k=1}^{r} \frac{1}{\forall} \frac{d}{dt} \left(m_p(k) V_i(k) \right) \dot{N}(k) \Delta t \tag{3.46}$$

$$\dot{S}_E = \sum_{k=1}^{r} \frac{1}{\forall} \frac{d}{dt} \left(h \pi d_p^2 \left(T_g - T_p \right) + \varepsilon_p \pi d_p^2 \sigma \left(\theta_R^4 - T_p^4 \right) \right) \dot{N}(k) \Delta t \tag{3.47}$$

where $\forall$ is the volume of a computational cell which contains the particle class from 1 to r

during a time interval of Δt. The rate of particle number (the number of particles flowing per unit time) of a given class is obtained as

$$N\left(k\right) = \frac{m_{f,in}dG'\left\{d_i\left(k\right)\right\}}{m_{p,i}\left(k\right)}$$

(3.48)

3.4 NOₓ Formation Modelling

NOₓ in combustion processes can be formed by four routes: thermal (by oxidation of N_2 in the oxidizer at temperatures above 1800 K), prompt (by hydrocarbon radicals attacking N_2 to form cyanide species and then to NO at the flame front), fuel (by oxidation of nitrogen contained in the fuel) and by means of N_2O. Compared to other species NOₓ concentrations are usually small and they do not affect flow field variables to a large extent. Hence, NOₓ concentrations are computed using post-processing after converged combustion flow field solution is obtained. The NOₓ model involves solving three transport equations for the mass fraction of NO, HCN and NH_3.

$$\frac{\partial}{\partial t}\left(\rho Y_{NO}\right) + \nabla.\left(\rho \vec{v} Y_{NO}\right) = \nabla.\left(\rho D \nabla Y_{NO}\right) + S_{NO}$$

(3.49)

$$\frac{\partial}{\partial t}\left(\rho Y_{HCN}\right) + \nabla.\left(\rho \vec{v} Y_{HCN}\right) = \nabla.\left(\rho D \nabla Y_{HCN}\right) + S_{HCN}$$

(3.50)

$$\frac{\partial}{\partial t}\left(\rho Y_{NH_3}\right) + \nabla.\left(\rho \vec{v} Y_{NH_3}\right) = \nabla.\left(\rho D \nabla Y_{NH_3}\right) + S_{NH_3}$$

(3.51)

Under oxy-coal combustion cases, due to absence of nitrogen in the oxidizer (air is replaced by mixture of O_2/CO_2), the NOₓ produced by thermal, prompt and N_2O routes

reduces to almost zero and only fuel NO_x contributes to total NO_x produced (Perrone et al., 2018; Tu et al., 2015).
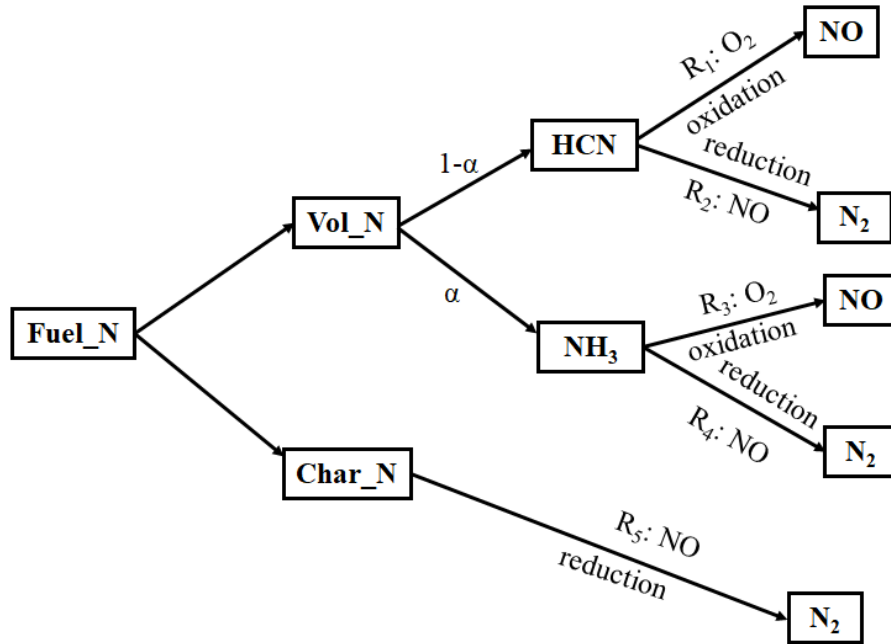
Fig. 3.2. Schematic diagram of the formation/destruction of fuel NO_x (Adopted from Al-Abbas et al., 2012)

The nitrogen contained in coal is distributed in volatile matter (VM) and char. The formation/destruction route of fuel NO_x is still research topic. The conversion of nitrogen contained in coal to NO_x has dependency on initial nitrogen concentration in coal and combustion characteristics. Based on the fuel NO_x mechanism, which has been widely accepted among researchers working on this area, we have shown NO_x formation/destruction pathway in Fig. 3.2.

The main fuel NO_x reactions can be presented in following form:

$$HCN + 1.25O_2 \rightarrow NO + CO + 0.5H_2O \tag{3.52}$$

$$HCN + 1.5NO \rightarrow 1.25N_2 + CO + 0.5H_2O \tag{3.53}$$

$$NH_3 + 1.25O_2 \rightarrow NO + 1.5H_2O \tag{3.54}$$

$$NH_3 + 1.5NO \rightarrow 1.5N_2 + 1.5H_2O \tag{3.55}$$

$$C_{char} + NO \rightarrow 0.5N_2 + CO \tag{3.56}$$

The oxidation and reduction processes are represented by eq[n] (3.52-3.55), whereas eq[n] (3.56) represent reduction of NO to N_2 by means of additional heterogeneous reaction. The rates of depletion of HCN and NH_3 are given by De Soete (1975), whereas rate of heterogeneous reduction of NO to N_2 by Levy et al. (1981).

$$
\begin{aligned}
R_1 &= 1.0 \times 10^{10} X_{HCN} X_{O_2}^a \exp\left(-\frac{33730.829}{T}\right) \\
R_2 &= 3.0 \times 10^{12} X_{HCN} X_{NO} \exp\left(-\frac{30206.713}{T}\right) \\
R_3 &= 4.0 \times 10^6 X_{NH_3} X_{O_2}^a \exp\left(-\frac{16110.247}{T}\right) \\
R_4 &= 1.8 \times 10^8 X_{NH_3} X_{NO} \exp\left(-\frac{13593.021}{T}\right) \\
R_5 &= 4.8 \times 10^4 \exp\left(-\frac{34.70}{RT}\right) A_E P_{NO}
\end{aligned}
\tag{3.57}
$$

Where R_{1-4} (in units of $s^{-1)}$ and R_5 (in mol s^{-1}) represent rates of conversion of eq[n] (3.52-3.55) and coefficient rate of char/NO reaction, respectively. X (in mol m^{-3}) represents species mole fraction. A_E and P_{NO} represent external char surface area and bulk pressure of NO. *a* represents reaction order for oxygen and the mathematical expression for *a* is given as:

$$
a = \begin{cases}
1.0 & X_{O_2} \leq 4.1 \times 10^{-3} \\
-3.95 - 0.9 \ln X_{O_2} & 4.1 \times 10^{-3} \leq X_{O_2} \leq 1.11 \times 10^{-2} \\
-3.95 - 0.9 \ln X_{O_2} & 1.11 \times 10^{-2} < X_{O_2} < 0.03 \\
0 & X_{O_2} \geq 0.03
\end{cases}
\tag{3.58}
$$

The expressions for source terms of NO, HCN and NH₃, which needs to be implemented in transport equations for the prediction of fuel NOₓ can be given as:

$$S_{HCN} = S_{HCN,P} + S_{HCN,1b} + S_{HCN,2b}$$
$$S_{NH_3} = S_{NH_3,P} + S_{NH_3,1b} + S_{NH_3,2b}$$
$$S_{NO} = S_{char,NO} + S_{NO,1} + S_{NO,2} + S_{NO,3}$$

(3.59)

The nitrogen contained in coal is supposed to be equally distributed into volatile matter (VM) and char and exact amount can be found from the proximate data of coal. Based on the available literature on fuel NOₓ modelling, we have assumed that nitrogen contained in VM is released as NH₃ and HCN mixture having NH₃/HCN ratio (α) of 9:1 (Al-Abbas and Naser, 2012; Jovanović et al., 2019). NH₃ and HCN released from volatile matter is further oxidized/reduced to form NO or N₂. Nitrogen contained in char is directedly oxidized to NO. Therefore, the NH₃/HCN ratio (α) is taken into account during the estimation of source terms of production rates of HCN and NH₃.

$$S_{HCN,P} = \frac{(1-\alpha)S_{vol}Y_{N,fuel}M_{HCN}}{M_N \Delta V} + \frac{S_{char}Y_{N,fuel}M_{HCN}}{M_N \Delta V}$$

$$S_{NH_3,P} = \frac{\alpha S_{vol}Y_{N,fuel}M_{NH_3}}{M_N \Delta V} + \frac{S_{char}Y_{N,fuel}M_{NH_3}}{M_N \Delta V}$$

(3.60)

$S_{HCN,P}$ and $S_{NH3,P}$ represents HCN and NH₃ source teems of thermal decomposition of coal. The devolatilization and char burnout rates are represented by S_{vol} and S_{char}. Y_N, represents coal_N mass fraction. M_N, M_{HCN} and M_{NH3} represents molecular weight of N, HCN and NH₃.

The consumption rates of HCN and NH₃ can be given by:

$$S_{HCN,1b} = -R_1 \frac{M_{HCN}P}{R\overline{T}}$$

$$S_{HCN,2b} = -R_2 \frac{M_{HCN}P}{R\overline{T}}$$

$$S_{NH_3,1b} = -R_3 \frac{M_{NH_3}P}{R\overline{T}}$$

$$S_{NH_3,2b} = -R_4 \frac{M_{NH_3}P}{R\overline{T}}$$

(3.61)

Where $S_{HCN,1b}$, $S_{HCN,2b}$ and $S_{NH3,1b}$, $S_{NH3,2b}$ represent rate of HCN and NH_3 consumption in eq^n (3.52-3.53) and eq^n (3.54-3.55) respectively. P and $\overline{T}$ represent pressure and mean temperature.

At last, as given in eq^n (3.59), the NO source term can be estimated as follows:

$$S_{char,NO} = \frac{S_{char}Y_{N,fuel}M_{NO}}{M_N \Delta V}$$

$$S_{NO,1} = R_1 \frac{M_{NO}P}{R\overline{T}} - R_2 \frac{M_{NO}P}{R\overline{T}}$$

$$S_{NO,2} = R_3 \frac{M_{NO}P}{R\overline{T}} - R_4 \frac{M_{NO}P}{R\overline{T}}$$

(3.62)

Where $S_{char,\ NO}$ is rate of production of NO from char reaction. $S_{NO,1}$ and $S_{NO,2}$ represent production and destruction rates of NO via eq^n (3.52-3.53) for HCN and via eq^n (3.54-3.55) for NH_3.

3.5 Grid Independence Study and Validation of the Numerical Model

This section presents grid independence study and experimental validation of the numerical model. The prediction of current RANS numerical results are compared with the

experimental results of Toporov et al. (2008) and numerical LES results of Warzecha and Boguslawski (2014a).

3.5.1 Grid Independence Study
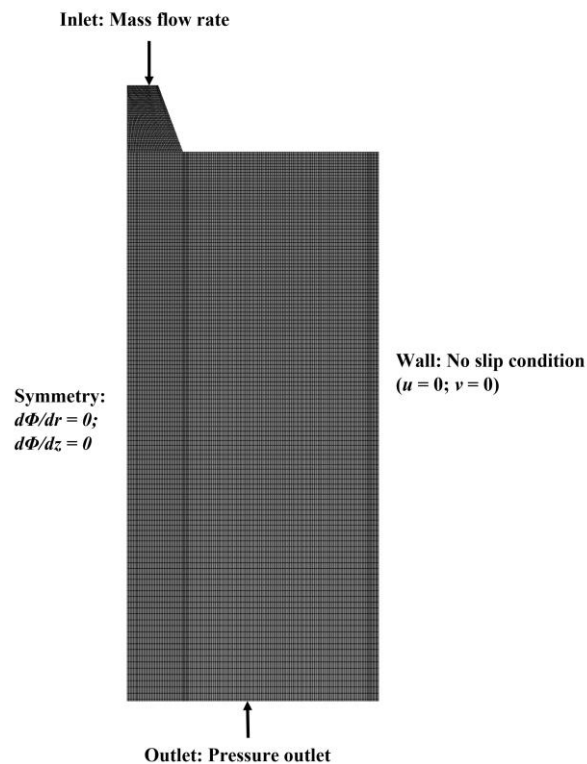
Fig. 3.3. Computational mesh used in the present 2D axisymmetric simulation

A 2 D axisymmetric structured mesh of combustor shown in Fig. 3.1 has been generated. 2D axisymmetric mesh used in the study is shown in Fig. 3.3. For the grid independence test, the mesh having 27000, 33000 and 40000 cells have been selected. Fig. 3.4 shows the axial velocity and temperature distribution along radial positions at axial location 0.05 m from burner exit for different grids. From the Fig. 3.4, it can be seen that the velocity and temperature profile have insignificant influence of number of grids. Therefore, mesh

having 33000 cells have been selected. In order to achieve a more accurate results the grid

density has been improved adjacent to the burner and along the axis.

(a)   **(b)**
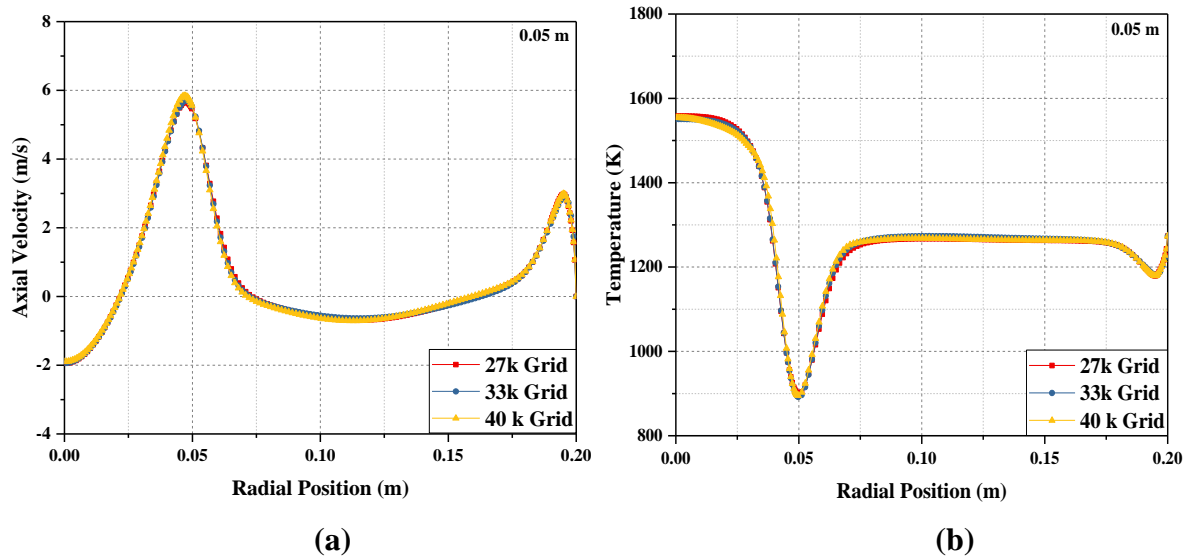
Fig. 3.4. Radial profile of **(a)** axial velocity (m/s) and **(b)** temperature (K) at axial location 0.05 m for grid independence test

3.5.2 Validation of Numerical Model

Fig. 3.5 shows the comparison of RANS prediction of the radial profile of axial velocity

with the experimental result of Toporov et al. (2008) and LES simulation result of

Warzecha and Boguslawski (2014a) at four different axial locations from burner exit. The

RANS prediction of axial velocity profile has an acceptable agreement with the

experimental results at 0.025 m axial location from burner exit (Fig. 3.5 a). The standard *k-ε* model has underpredicted peak axial velocity by 8%, whereas other RANS turbulence

models and the LES model of Warzecha and Boguslawski (2014a) overpredicted peak axial

velocity by 8-12% deviation with the experimental results of Toporov et al. (2008).
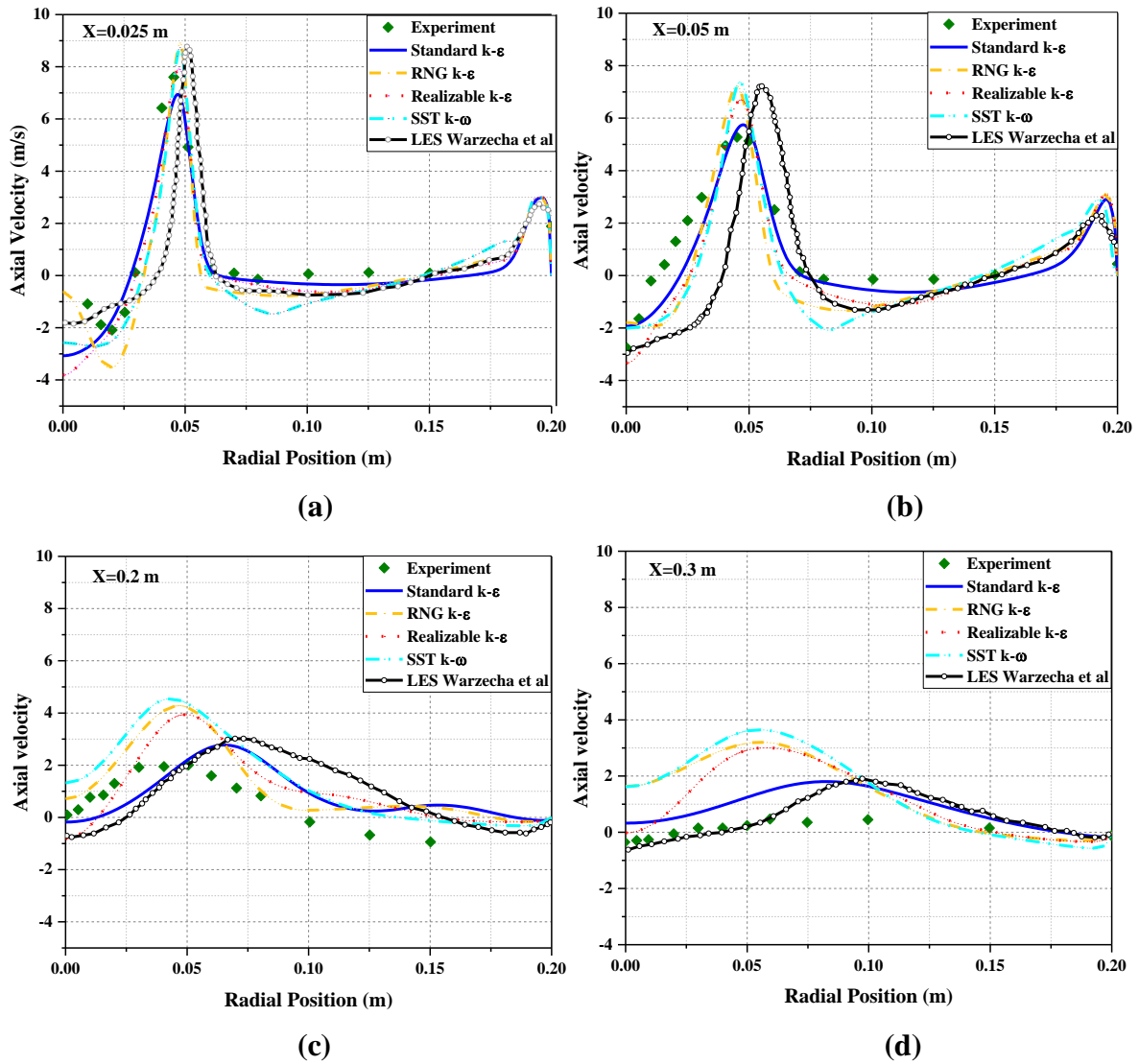
Fig. 3.5. Comparison of RANS prediction of axial velocity (m/s) with LES result and experimental data at different axial locations from burner **(a)** 0.025 m **(b)** 0.05 m **(c)** 0.2 m and **(d)** 0.3 m

From Fig.3.5 (b) it can be seen that the standard *k-ε* model has captured axial velocity profile more accurately than the other RANS turbulence models at 0.05 m axial location from burner exit. At this axial location, other RANS models and LES model of Warzecha and Boguslawski (2014a) overpredicted peak axial velocity. Fig. 3.5 (c) and Fig. 3.5 (d) show that the overall trend of axial velocity profile has been captured at axial location 0.2

m and 0.3 m, respectively by the RANS models having slight discrepancies with the experimental result at certain points. At both the locations slightly radially shifted axial velocity profile with higher magnitude has been observed due to the prediction of wider flames. The discrepancies in RANS model prediction and experimental result of axial velocity has been associated due to the inability of the model to capture turbulent fluctuations of swirl flow and wrongly interpreted size and shape of internal recirculation zone (IRZ). The constant value of the axial and tangential velocity at the burner exit has been assumed due to unavailability of axial velocity profile from the experimentation, which has also attributed to discrepancies between RANS predictions and experimental results.

Fig. 3.6 compares the RANS prediction of the radial profile of tangential velocity with the experimental result of Toporov et al. (2008) at four different axial locations from the burner exit. From Fig. 3.6 (a), it can be seen that peak negative tangential has been found at the radial distance 0.05 m. The RANS turbulent models prediction of tangential velocity cannot be compared with measured data for a radial distance less than 0.05 m due to unavailability of experimental result. The lower magnitude of tangential velocity has been observed at the radial distance 0.05<R<0.15 m. From Fig. 3.6 (b) it can be seen that the standard k-ε model has slightly underpredicted the peak negative tangential velocity. In contrast, other RANS turbulence models overpredicted at 0.05 m axial location from burner exit. The peak negative tangential velocity has been overpredicted by RNG k-ε, Realizable k-ε and SST k-ω models by 60%, 6% and 20%, respectively than the experimental result. Fig. 3.6 (c) and Fig. 3.6 (d) shows that the tangential velocity profile has been

overpredicted at the inner radial positions 0<R<0.1 m, at axial locations 0.2 m and 0.3 m. At both these locations, the RANS models have predicted tangential velocity profile more accurately towards outer radial locations (0.15<R<0.2 m). Chen and Ghoniem (2012) tried to identify the source of this discrepancy by comparing the total gas mass flow rate and the total angular momentum in the experimental and simulation results. They found that the measured mass flow rate downstream is significantly lower than the total burner mass flow rate. That's why the measurement showed very smaller tangential velocity at downstream.
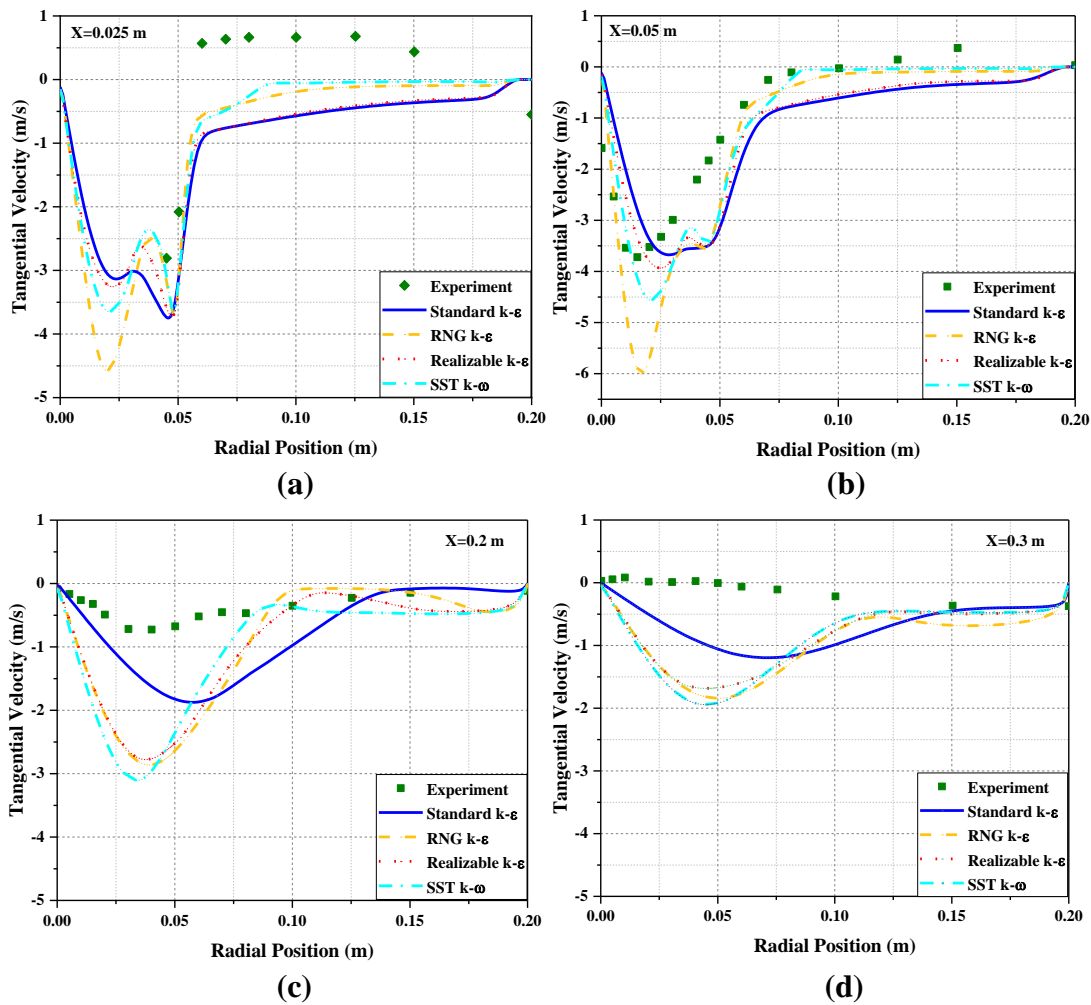
Fig. 3.6. Comparison of RANS prediction of tangential velocity (m/s) with experimental data at different axial locations from burner **(a)** 0.025 m **(b)** 0.05 m **(c)** 0.2 m and **(d)** 0.3 m
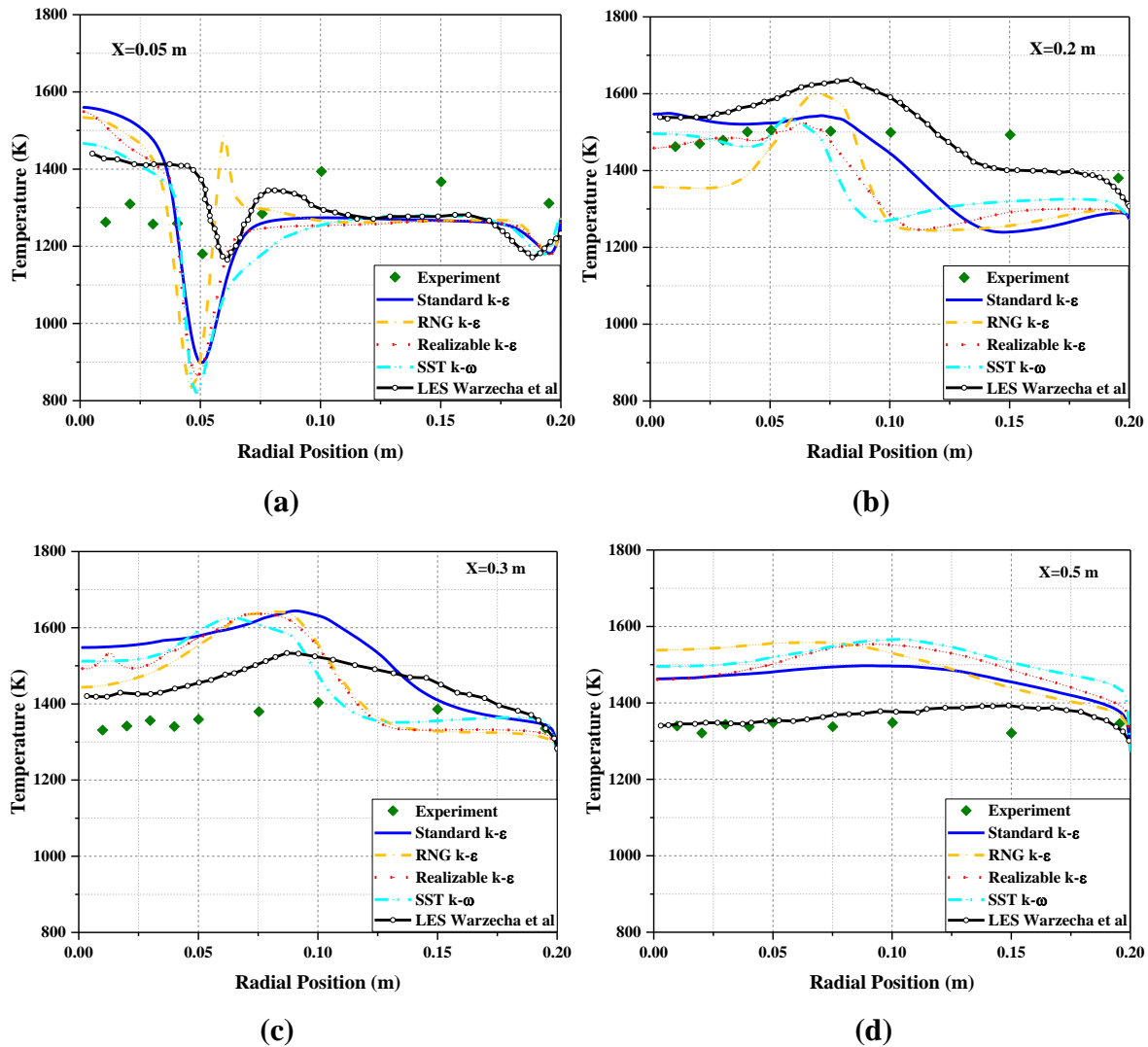
Fig. 3.7. Comparison of RANS prediction of temperature (K) with LES result and experimental data at different axial locations from burner **(a)** 0.05 m **(b)** 0.2 m **(c)** 0.3 m and **(d)** 0.5 m

Fig. 3.7 compares the RANS prediction of the radial profile of temperature with the experimental result of Toporov et al. (2008) and LES simulation results of Warzecha and Boguslawski (2014a) at four different axial locations from burner exit. It can be seen that both RANS and LES models have some discrepancies with the experimental result of Toporov et al. (2008), especially close to the burner exit. Fig. 3.7 (a) shows that the

maximum difference between RANS turbulence models predictions and the experimental result has been obtained at a radial distance of 0.05 m (temperature minima has been found). Volatile combustion and product recirculation in the internal recirculation zone takes place in the region adjacent to burner exit. The differences between numerical and experimental results have been attributed due to the inability of the model to predict the strong recirculation zone, which has been formed by the distribution of burner cold stream. At axial location 0.2 m, towards the inner radial positions 0<R<0.075 m, SST k-ω and Realizable k-ε model have predicted temperature distribution more accurately. Whereas, towards the outer radial positions R>0.1 m, LES has a comparatively better prediction of temperature profile than the RANS turbulence models. Fig. 3.7 (c) and Fig. 3.7 (d) show that the RANS turbulence models have been able to capture the overall trend of temperature profile having variations in the range of 5-15% with the experimental results. Fig. 3.8 compares the RANS prediction of the radial profile of oxygen mole fraction with the experimental result of Toporov et al. (2008) and LES simulation results of Warzecha and Boguslawski (2014a) at four different axial locations from burner exit. Fig. 3.8 (a) shows that the inner radial positions 0<R<0.05 m, have comparatively very less value of oxygen mole fraction at 0.05 m axial location. Toward outer radial positions 0.075<R<0.2 m, significant deviation of 30-35% between experimental results and RANS prediction have been found. Fig. 3.8 (b) displays that the standard k-ε model has more accurately predicted oxygen mole fraction at inner radial positions 0<R<0.075 m, whereas toward the outer radial positions RANS turbulence models overpredicted and LES underpredicted oxygen mole fraction profile. Fig. 3.8 (c) and Fig. 3.8 (d) show that the overall trend of

oxygen mole fraction profile has been accurately captured by RANS turbulence models having slight deviations towards the outer radial positions at axial locations 0.3 m and 0.5 m from the burner.

(a)

(b)

(c)

(d)
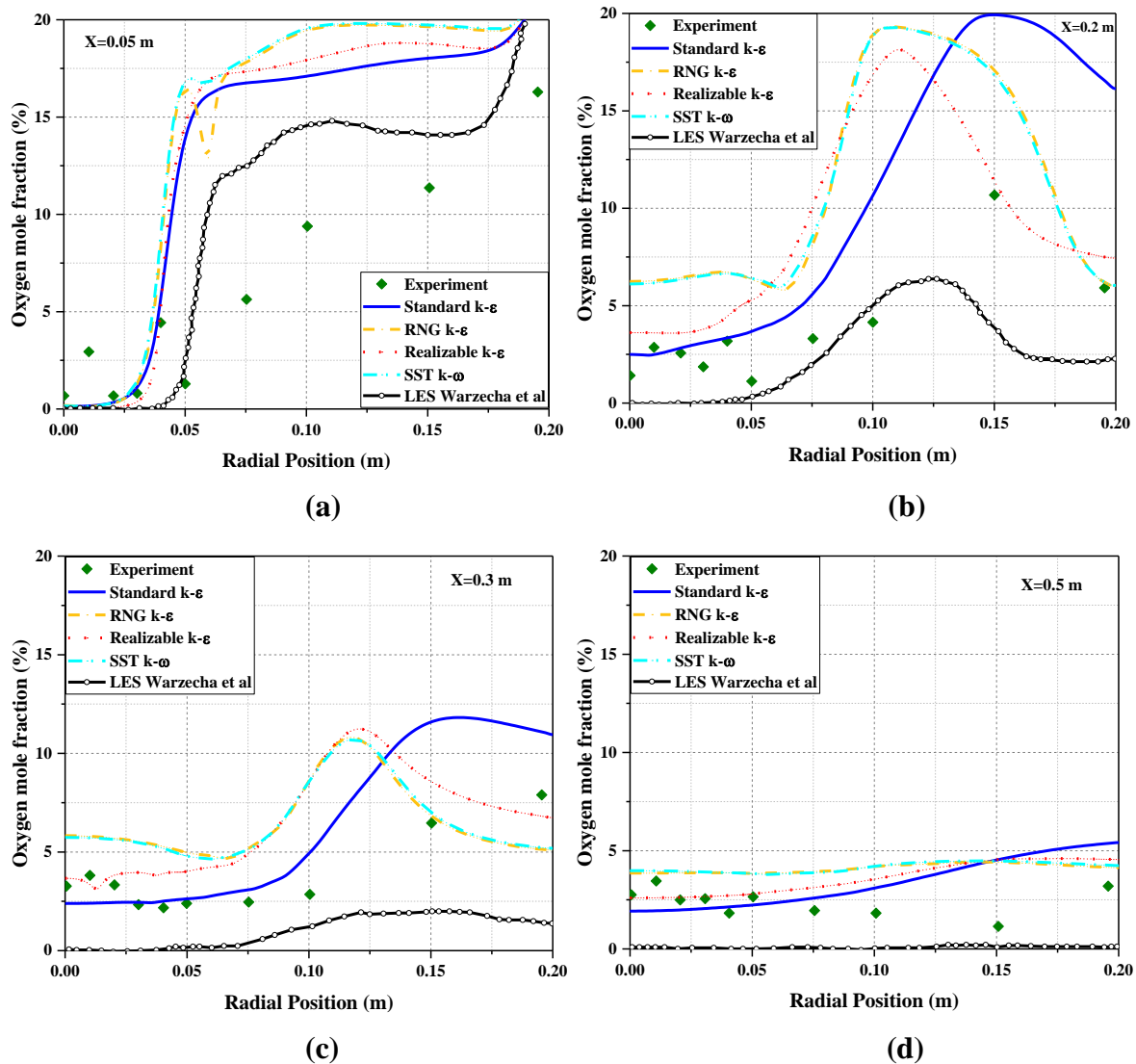
Fig. 3.8. Comparison of RANS prediction of O_2 mole fraction (%) with LES result and experimental data at different axial locations from burner **(a)** 0.05 m **(b)** 0.2 m **(c)** 0.3 m and **(d)** 0.5 m

The significant deviations in oxygen mole fraction distribution are observed for various RANS based turbulence models due to their differently predicted flow field and mixing

process. More significant deviations between the model prediction and experimental values are found towards the outer radial locations. Staging stream is injected through the outer radial wall to maintain the stoichiometry of the burner. Due to improper mixing between the streams, overprediction of oxygen mole fraction is observed towards outer radial positions.

3.5.3 Summary

Thus, based on section 3.5.2, overall, an acceptable agreement between the experimental and numerical results have been found. Although there are some discrepancies between current RANS prediction and experimental data for temperature and oxygen mole fraction close to the burner, the current developed model is able to capture qualitative trend at all axial locations. Thus, the current simplified model is good enough without losing much accuracy compared to LES modelling. The predicted reactive flow field, temperature and oxygen mole fraction distributions are not much affected by changing RANS based turbulence models. Hence, the standard k-ε model has been selected for further parametric simulations as it requires lesser computational time compared to other RANS turbulence models.